Quantum non-demolition measurement of an electron spin qubit

Takashi Nakajima [1,9]*, Akito Noiri [1,9], Jun Yoneda [1], Matthieu R. Delbecq [1,7], Peter Stano [1,2,3], Tomohiro Otsuka [1,4,8], Kenta Takeda [1], Shinichi Amaha [1], Giles Allison[1], Kento Kawasaki[3], Arne Ludwig [5], Andreas D. Wieck [5], Daniel Loss [1,6] and Seigo Tarucha[1,3]*
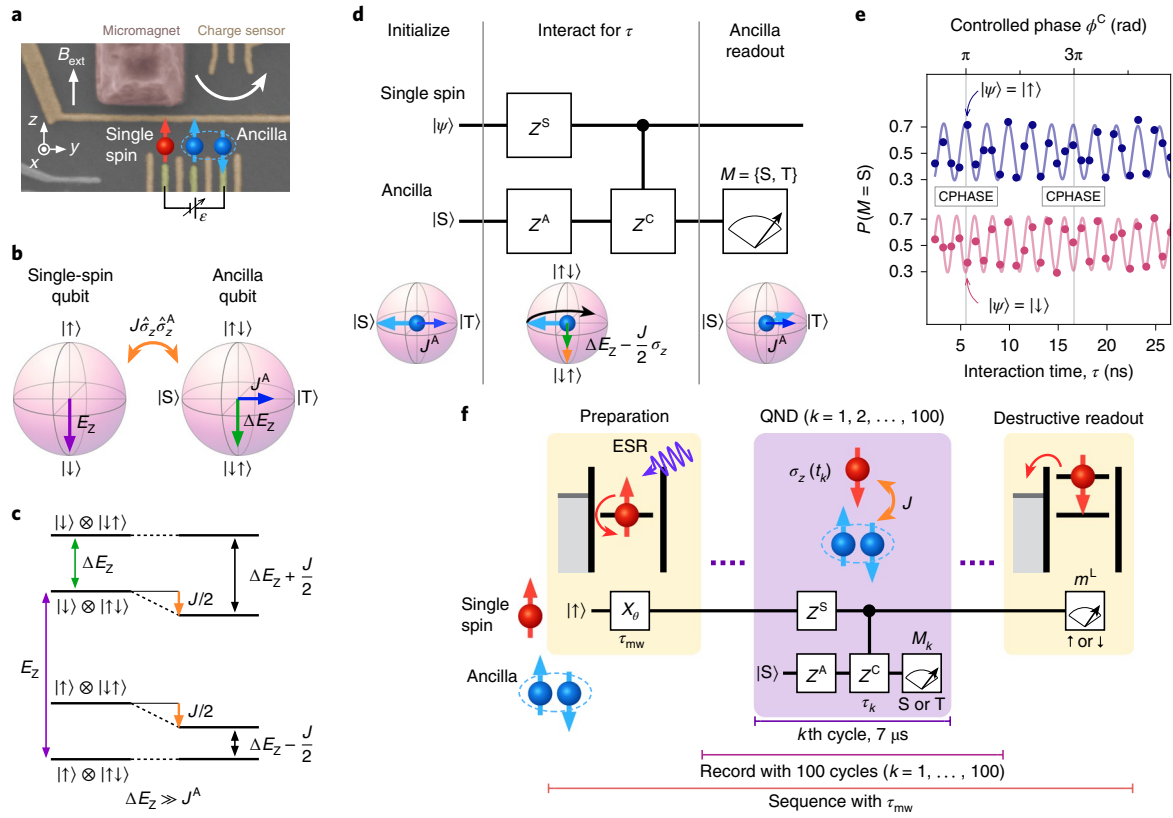
Measurements of quantum systems inevitably involve disturbance in various forms. Within the limits imposed by quantum mechanics, there exists an ideal projective measurement that does not introduce a back action on the measured observable, known as a quantum non-demolition (QND) measurement[1,2]. Here we demonstrate an all-electrical QND measurement of a single electron spin in a gate-defined quantum dot. We entangle the single spin with a two-electron, singlet–triplet ancilla qubit via the exchange interaction[3,4] and then read out the ancilla in a single shot. This procedure realizes a disturbance-free projective measurement of the single spin at a rate two orders of magnitude faster than its relaxation. The QND nature of the measurement protocol[5,6] enables enhancement of the overall measurement fidelity by repeating the protocol. We demonstrate a monotonic increase of the fidelity over 100 repetitions against arbitrary input states. Our analysis based on statistical inference is tolerant to the presence of the relaxation and dephasing. We further exemplify the QND character of the measurement by observing spontaneous flips (quantum jumps)[7] of a single electron spin. Combined with the high-fidelity control of spin qubits[8-13], these results will allow for various measurement-based quantum state manipulations including quantum error correction protocols[14].

Spin-based qubits in semiconductor quantum dots[15] are a promising platform for universal quantum computing due to their high-fidelity coherent control, scalability and industry-compatible architecture. One of the current bottlenecks for the single-electron spin qubit is the fidelity and speed of its initialization and measurement. This limitation is due to the inherently destructive nature of the single-shot measurement method currently used[16]. Quantum non-demolition (QND) measurements offer unique possibilities to overcome this issue using techniques such as repetitive readout[6] and feedback-controlled initialization[17]. However, a QND measurement has remained elusive for electron spins, in contrast to other solid-state systems such as superconducting qubits[5], or nuclear spins in diamond colour centres[18,19] and silicon donors[20]. While particular types of photonic readout of electron spins[7,21,22] can, in principle, be QND, their QND nature has not been demonstrated so far. Moreover, QND measurement via an ancillary qubit is crucial[14] for measurement-based quantum algorithms including quantum error correction codes.

We use a readout ancilla based on a singlet–triplet qubit[23] to demonstrate the QND measurement of a single electron spin in a GaAs/AlGaAs triple quantum dot (TQD) device (Fig. 1a,b). The single-spin eigenstates $|\uparrow\rangle$ and $|\downarrow\rangle$ of the electron in the left dot serve as a natural basis for the spin qubit. The Hamiltonian is written as $\hat{H}^{S} = -E_Z \hat{\sigma}_z/2$ using the Zeeman energy E_Z and the Pauli operator $\hat{\sigma}_z$, with $\sigma_z = \pm 1$ denoting its eigenvalue. The ancilla qubit is encoded in a two-dimensional space spanned by $|\uparrow\downarrow\rangle$ and $|\downarrow\uparrow\rangle$, where the first and second arrow denote the electron spin in the centre and right dots (both singly occupied), respectively. Using the pseudo-spin operators $\hat{\sigma}_i^A$ with $i \in \{x, y, z\}$ for these two basis states, the corresponding Hamiltonian is $\hat{H}^A = -\Delta E_Z \hat{\sigma}_z^A/2 + J^A \hat{\sigma}_x^A/2$, where ΔE_Z and J^A are the Zeeman field gradient and the exchange coupling, respectively, between the centre and right dots. The ancilla measurement is done by projecting it onto $|S\rangle = \frac{1}{\sqrt{2}}(|\uparrow\downarrow\rangle - |\downarrow\uparrow\rangle)$ or $|T\rangle = \frac{1}{\sqrt{2}}(|\uparrow\downarrow\rangle + |\downarrow\uparrow\rangle)$ (eigenstates of $\hat{\sigma}_x^A$). In this hybrid system[3,4], the energy splittings are gate-tunable due to the presence of the interaction term $\hat{H}^{int} = \frac{J}{4}(\hat{\sigma}_z \hat{\sigma}_z^A - 1)$ (Fig. 1c). Namely, the inter-qubit exchange J is controlled through the wavefunction overlap between the left and centre dots. Viewed from the ancilla qubit, $\hat{H}^{int}$ changes the energy splitting of $|\uparrow\downarrow\rangle$ and $|\downarrow\uparrow\rangle$ by $-J\sigma_z/2$, making it dependent on the single-spin state. The dependence allows us to entangle the two qubits and extract information on the single spin via the readout of the ancilla in the following steps (Fig. 1d). Suppose that the single spin starts in an initial state $|\psi\rangle = \alpha|\uparrow\rangle + \beta|\downarrow\rangle$, and is decoupled from the ancilla ($J = 0$). We first initialize the ancilla to its ground state $|S\rangle$ (an eigenstate of $\hat{\sigma}_x^A$) by temporarily increasing J^A. After that, we change the energy detunings between neighbouring dots to turn J^A off and J on[4]. Now that the ancilla eigenstates are $|\uparrow\downarrow\rangle$ and $|\downarrow\uparrow\rangle$ split by $\Delta E_Z - J\sigma_z/2$, the ancilla precesses in a plane of the Bloch sphere containing $|S\rangle$ and $|T\rangle$. After time τ, which we call the interaction time, the precession angle (or the relative phase of $|\uparrow\downarrow\rangle$ and $|\downarrow\uparrow\rangle$) becomes $\phi^A - \phi^C \sigma_z/2$, where we define phases independent of and dependent on σ_z, $\phi^A = \Delta E_Z \tau/\hbar + \phi_0$ and $\phi^C = J\tau/\hbar$, respectively (ϕ_0 is an offset due to the control pulse, as described in the Methods). The precession is terminated by a projective measurement of the ancilla onto the $|S\rangle$–$|T\rangle$ basis (spin blockade), giving an outcome $M \in \{S, T\}$. Figure 1e shows an example of the τ-dependence of the probability of finding a singlet $P(M = S)$. It reflects the growth of phases $\phi^A + \phi^C/2$ for $|\psi\rangle = |\downarrow\rangle$ and $\phi^A - \phi^C/2$ for $|\uparrow\rangle$, respectively. The ancilla measurement is most informative about the single-spin state if the two

Fig. 1 | QND readout of a single electron spin via an ancillary qubit. a, False-coloured scanning electron micrograph image of the device. The cobalt micromagnet deposited on the wafer surface is magnetized by an in-plane magnetic field $B_{ext} = 3.155\,T$ to induce the Zeeman field gradient ΔE_Z and the slanting field for the MM-ESR. The TQD charge configuration is probed by a proximal quantum dot charge sensor using radiofrequency reflectometry[32]. **b,c**, Schematic of a single electron spin coupled with an ancilla by the exchange interaction J (**b**) and the corresponding energy diagram (**c**). **d**, QND measurement protocol. The ancilla is entangled with the single spin in an arbitrary input state $|\psi\rangle$ by a controlled phase rotation and then projected onto either the singlet (S) or triplet (T) state. Symbols Z^S, Z^A and Z^C represent Z rotations (see Methods). **e**, Example of singlet–triplet precession of the ancilla showing the spin-dependent phase. The singlet probability of the ancilla is measured as a function of the interaction time τ_k for $|\psi\rangle = |\uparrow\rangle$ (blue circles) and $|\psi\rangle = |\downarrow\rangle$ (red circles) input states. Solid curves are fits to the data. Vertical grey lines indicate values of τ satisfying $\phi^C = (2\ell + 1)\pi$ and $-\phi^A + \phi^C/2 = 2m\pi$ ($\ell, m \in \mathbb{Z}$, see Methods). **f**, Experimental sequence for repeated QND measurement and a subsequent destructive readout of the single spin. After preparing an input spin with $\langle\sigma_z(0)\rangle$ by the MM-ESR, 100 QND readout cycles with varied τ_k are performed, each of which takes 7 μs. Finally, the single spin is read out by energy-selective tunnelling[16].

qubits are maximally entangled, that is, for $\phi^C = (2\ell + 1)\pi$ ($\ell \in \mathbb{Z}$). If $\phi^C = \pi$ and $\phi^A = \pi/2$, for example, the ancilla measurement realizes a projective measurement of the spin operator $\hat{\sigma}_z$ with the outcome +1 for $M = $ S and -1 for $M = $ T. Since the measurement protocol neither perturbs the evolution of $\hat{\sigma}_z$, expressed as $[\hat{H}^{int}, \hat{\sigma}_z] = 0$, nor increases the uncertainty of $\hat{\sigma}_z$, expressed as $[\hat{\sigma}_z, \hat{H}^S] = 0$, it meets the definition of a QND measurement[2].

The experiment consists of repeating the sequence shown in Fig. 1f. It begins with preparation of the single spin followed by QND readout cycles (indexed by integer k) and finishes with a destructive readout of the single spin. In the preparation step, the single spin is reset to $|\uparrow\rangle$ by energy-selective tunnelling[16] and is initialized to a desired state $|\psi\rangle$ by Rabi rotation, utilizing the micromagnet electron spin resonance (MM-ESR)[24,25]. The microwave burst duration τ_{mw} sets the expectation value of the initial spin state, denoted as $\langle\hat{\sigma}_z(t = 0)\rangle \in [-1, 1]$. The kth QND readout cycle is performed at time $t = t_k$ using the interaction time $\tau = \tau_k$, to infer the unknown value of $\sigma_z(t_k)$ from the ancilla measurement result M_k. Our statistical procedure (described below) assigns $m_k = \pm1$ as the estimator of $\sigma_z(t_k)$. We perform 100 consecutive cycles, $k = 1, 2,..., 100$, varying τ_k linearly as $\tau_k = k \times 0.83\,ns + \tau_0$. Here, the time step is chosen as the maximum resolution of the hardware and $\tau_0 = 1.5\,ns$

accounts for the pulse ramp time (see Methods). A data set of 100 cycles, each of which takes 7 μs, is referred to as a record in the following. The sequence is finished by a destructive measurement[16] of the single spin $\sigma_z(t = 700\,\mu s)$, with an outcome denoted by m^L. The whole sequence is run 50 times with τ_{mw} varied from 10 ns to 500 ns. The block of 50 sequences is repeated 800 times.

In the kth readout cycle, we determine the estimator of the spin $\sigma_z(t_k)$ by comparing probabilities $P(\sigma_z|M_k)$ of finding $\sigma_z = \pm1$ conditioned on the ancilla measurement outcome M_k. That is, we assign the estimator to be the value m_k that satisfies $P(m_k|M_k) > P(-m_k|M_k)$. The inequality is evaluated using Bayes' theorem, cast as $\frac{P(m_k | M_k)}{P(-m_k | M_k)} = \frac{P(M_k | m_k)}{P(M_k | -m_k)}$, where $P(M_k|\sigma_z)$ is the likelihood of finding an ancilla outcome M_k for given σ_z. An example of the measured likelihood is plotted in Fig. 1e. Based on such measurements, we adopt the formula[4]

$$P(M_k = S|\sigma_z) = 1 - P(M_k = T|\sigma_z)$$
$$= a\cos(\phi^A - \phi^C\sigma_z/2)\exp[-(\tau_k/T_2^\star)^2] + b \tag{1}$$

Here, the ancilla dephasing within a record[26] is reflected by $T_2^\star$, while a and b parameterize imperfections of the protocol such as

the state preparation and measurement errors of the ancilla qubit, tilt of the qubit rotation axis while J is turned on, and leakage to non-qubit states. All parameters are recalibrated before every record (see Methods for details). Figure 2a shows the estimator $\langle m_k \rangle$ for $k=5$ ($\tau_k = 5.7$ ns) and the destructive readout result $\langle m^L \rangle$ as functions of the microwave burst time τ_{mw} ($\langle \cdots \rangle$ denotes ensemble averaging over the blocks). Both measurement outcomes exhibit clear Rabi oscillation of the single spin. The estimator $\langle m_k \rangle$ plotted as a function of k in Fig. 2b shows that the visibility of the Rabi oscillation reaches a maximum for $k=5$ where the two qubits are nearly fully entangled.

An essential figure of merit in the QND readout is the fidelity, which is the probability of obtaining a correct estimator value m_k when a qubit with a known eigenvalue of $\sigma_z(t_k)$ is given at the time of measurement t_k. However, evaluation of the fidelity requiring a perfectly known input state is impractical. Instead, we write the Rabi oscillation of the input as $(1 + \langle \sigma_z(t_k; \tau_{mw}) \rangle)/2 = A(t_k)e^{-(\tau_{mw}/T_2^{Rabi})^2}\cos(2\pi f_{Rabi}\tau_{mw} + \varphi) + B(t_k)$ to parameterize state preparation errors and the spin relaxation over time t_k by the amplitude $A(t_k)$ and the mean $B(t_k)$ along with the Rabi frequency f_{Rabi}, the Rabi damping time T_2^{Rabi} and a phase offset φ. By analysing the joint probabilities of the QND and destructive readouts, we separate the readout infidelities from the state preparation errors (see Methods for the detailed procedure). The extracted QND readout fidelities $\langle f_{\sigma,k} \rangle$ ($\sigma = \uparrow (\downarrow)$ for $\sigma_z(t_k) = +1 (-1)$ inputs) and the values of $A(t_k)$ and $B(t_k)$ are plotted in Fig. 2c. The fidelities $\langle f_{\sigma,k} \rangle$ show damped oscillations reflecting the accumulation of the controlled phase ϕ^C; they reach maxima (minima) when ϕ^C is an odd (even) multiple of π. The extracted fidelities agree very well with the numerical simulation (see Methods) plotted as the solid curves, reassuring us that we are extracting this key measurement characteristic correctly. Finally, we find that the spin relaxation and excitation times $T_\downarrow$ and $T_\uparrow$ extracted from the decay of $A(t_k)$ and $B(t_k)$ are much larger than the QND readout cycle time (7 μs). From this we conclude that the disturbance due to the readout protocol is small, as discussed below in more detail. This is the essential feature of the QND measurement, which allows one to enhance the readout fidelity by repeating the measurement of an observable.

To demonstrate the potential of repeated measurements, we use a set of measurement outcomes $\{M_k; k \in [1, n]\}$ obtained from n consecutive QND readout cycles to calculate q_n, a cumulative estimator for the initial value of the single spin. We use linearly varied τ_k to improve the protocol robustness as described below. Similarly as before, we obtain an estimator q_n from requiring $P(q_n|\{M_k\}) > P(-q_n|\{M_k\})$, where $P(\sigma_0|\{M_k\})$ is the probability of the single spin having an eigenvalue $\sigma_z(t=0) = \sigma_0$. The probability $P(\sigma_0|\{M_k\})$ is proportional to the likelihood

$$P(\{M_k\}|\sigma_0) = \sum_{\{\sigma_k\}}\left[\prod_{k=1}^{n} P(M_k|\sigma_k)P(\sigma_k|\sigma_{k-1})\right] \quad (2)$$

Here, $\sigma_k = \sigma_z(t_k)$ and $P(\sigma_k|\sigma_{k-1})$ are the transition probabilities for spin evolution between t_{k-1} and t_k (see equation (3) in the Methods). Summing over all possible realizations of the spin trajectories $\{\sigma_k\}$ is essential to achieve the optimal fidelity[27]. Figure 3 shows the visibility improvement of the detected Rabi oscillations with increasing n. The averaged fidelity of the cumulative readout, $\langle F_{\uparrow,n} + F_{\downarrow,n} \rangle/2$, shows monotonic increase from 0.63 for $n=1$ to 0.89 for $n=100$. We note that there is negligible increase of the fidelity beyond $n \gtrsim 60$ due to the single-spin relaxation: one can no longer gain information from the readout outcomes at times when the single-spin state is decorrelated with its initial state (see Supplementary Fig. 3 for the explicit evaluation of the correlation).

One would expect to achieve the highest cumulative-readout fidelity $F_{\sigma,n}$ by repeating cycles with a fixed τ_k such that the single-readout fidelity $f_{\sigma,k}$ is maximal. However, $f_{\sigma,k}$ is influenced by the
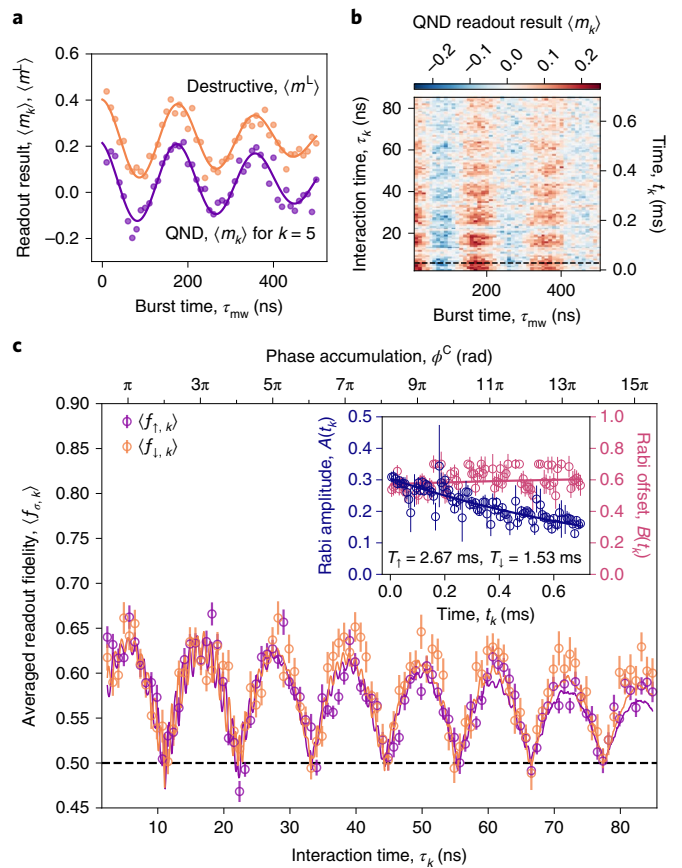
Fig. 2 | Demonstration of QND measurement and fidelity analysis. a, Averaged estimators for single QND readouts $\langle m_k \rangle$ (for $k=5$, $\tau_k = 5.7$ ns, where $\phi^C \approx \pi$) and destructive readout outcomes $\langle m^L \rangle$, plotted against the MM-ESR microwave burst time τ_{mw}. The solid curves are fits to the data with Rabi frequency $f_{Rabi} = 5.46 \pm 0.04$ MHz, Rabi damping time $T_2^{Rabi} = 526 \pm 42$ ns and phase offset $\varphi = 0.264 \pm 0.056$. **b**, Estimators versus burst time τ_{mw} and cycle index k. Both the interaction time $\tau_k = k \times 0.83$ ns $+ \tau_0$ (left axis) and the laboratory time $t_k = (k-1) \times 7$ μs (right axis) are specified by k. The horizontal black dashed line indicates $k=5$ shown in **a**. **c**, Averaged readout fidelities $\langle f_{\uparrow,k} \rangle$ and $\langle f_{\downarrow,k} \rangle$ (purple and orange circles, respectively) for the spin states in $\sigma_z(t_k) = \pm 1$, extracted from analysis of the joint probabilities as described in the Methods. Their envelopes decay with dephasing times $T_{2\uparrow}^* = 177$ ns and $T_{2\downarrow}^* = 212$ ns (see Methods). The solid curves show numerically simulated fidelities. The black dashed line shows a fidelity of 0.5 corresponding to random readout outcomes. Inset, amplitude $A(t_k)$ (left axis) and mean $B(t_k)$ (right axis) of the actual spin oscillation, decaying with time t_k. The solid curves are fits to the exponential, allowing us to extract the spin relaxation and excitation times $T_\downarrow = 1.53 \pm 0.07$ ms and $T_\uparrow = 2.67 \pm 0.11$ ms, respectively (see Methods). Error bars represent standard errors obtained from the least mean squares method.

ancilla phase ϕ^A fluctuating over the timescale of minutes due to the Overhauser field fluctuation[26,28]. For example, if $\phi^A = m\pi$ ($m \in \mathbb{Z}$), the projection angles of the ancilla against the $|S\rangle - |T\rangle$ measurement basis are equal for $\sigma_z = \pm 1$. Because $P(M|\sigma_z = +1) = P(M|\sigma_z = -1)$, one finds $f_{\sigma,k} = 0.5$, regardless of the value of ϕ^C. The uncontrolled fluctuations of ϕ^A therefore lead to large fluctuations of $f_{\sigma,k}$ and $F_{\sigma,n}$, as illustrated in the left inset of Fig. 3c. To mitigate this problem, we varied τ_k linearly with k, effectively averaging out the fluctuations. Consequently, $F_{\sigma,n}$ becomes more robust against the fluctuation as the number of cycles n increases (orange shaded region in Fig. 3c). On the other hand, the repetitive measurement with an optimal and
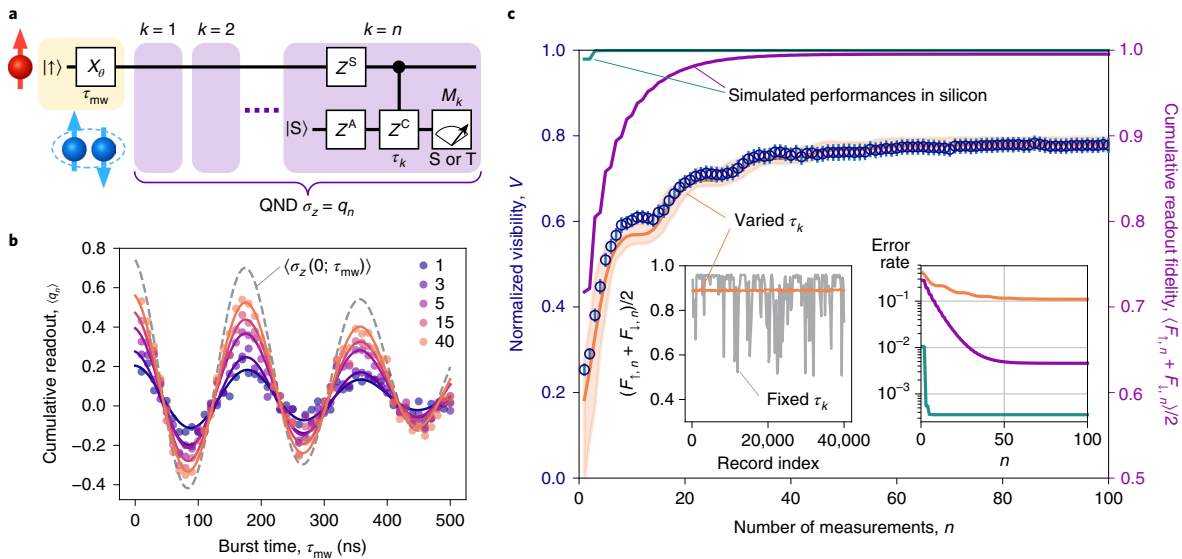
Fig. 3 | Fidelity boost in repetitive QND readouts. a, Sequence for preparing an input state and obtaining an estimator q_n for $\sigma_z(0;\tau_{mw})$ from consecutive QND readouts with linearly varied interaction time τ_k. **b**, Visibility enhancement of single-spin Rabi oscillations upon repeated QND readouts. As the readout fidelity increases with the number of consecutive measurements n, the measured Rabi oscillations (circles with colours for different values of n) approach the actual expectation value $\langle\sigma_z(0;\tau_{mw})\rangle$ (grey dashed curve). The solid curves are fits to the data. Note that even for a perfect measurement the visibility does not reach unity due to state preparation errors. **c**, Normalized visibility of the Rabi oscillations in **b** (blue circles, left axis) plotted against n. The normalized visibility is defined as $V_n = A_n/A(0)$, where A_n is the amplitude of the measured Rabi oscillation in **b** and $A(0) = 0.298$ is the amplitude of the actual spin oscillation at $t \to 0$ found in the inset of Fig. 2c. Error bars represent standard errors obtained from the fits in **b**. We relate the normalized visibility to the averaged fidelity by $(V_n + 1)/2 = \langle F_{\uparrow,n} + F_{\downarrow,n}\rangle/2$, which is shown on the right axis. The orange curve gives the simulated fidelity, with its variation due to the drift of ΔE_Z and ϕ_0 shown by the shaded region (bounded by its minima and maxima). The purple and green curves show the fidelities simulated for silicon quantum dots with ancilla readout visibilities of 44% and 98%, respectively, and with parameters[9,12] $T_2^\star = 1.84\ \mu s$, $T_\uparrow = 22\ ms$ and $T_\downarrow = 38\ ms$. Right inset, error rate $1 - \langle F_{\uparrow,n} + F_{\downarrow,n}\rangle/2$ for each case. Left inset, numerically simulated fidelities for $n = 100$ with a fixed interaction time of $\tau = 5.4\ ns$ for $\phi^C = \pi$ (grey) and with varied τ_k (orange), assuming that ΔE_Z fluctuates randomly according to a probability distribution seen in the experiment.

unvaried interaction time τ_k would be feasible in materials with less magnetic noise, such as silicon. Because the spin relaxation time also tends to be longer in those materials, the QND readout fidelity will be boosted significantly. The purple curve in Fig. 3c shows the fidelity estimated for typical parameters of a natural silicon quantum dot. Our simulations suggest that the fidelity reaches 99.5% at $n = 52$. Assuming the best readout visibility of 98% reported for a singlet–triplet qubit[29], the simulated fidelity, as shown by the green curve, reaches 99.96% at $n = 5$, well beyond the fault-tolerant threshold[30].

Finally, we demonstrate that we can follow the dynamics of an isolated electron spin in a quantum dot[7] using the QND measurement. As shown in Fig. 4, spontaneous spin-flip events can be revealed by continuously monitoring the cumulative estimators. The statistics of the dwell times, acquired during the total acquisition time of 1,000 s, reveal the spin relaxation and excitation times $T_\downarrow = 1.57\ ms$ and $T_\uparrow = 6.42\ ms$. Those values give an upper bound of the measurement-induced spin-flip rate of 0.3% per cycle (or 27% per record). Such disturbance could be caused by, for example, state leakage or the spin-electric coupling to the measurement pulse. However, these would perturb the spin states randomly, leading to the expectation $T_\uparrow \approx T_\downarrow$. Because we do not observe such a relation, we conclude that the relaxation time $T_\downarrow$ is dominated by the spin–environment coupling rather than the measurement protocol. Indeed, the $T_\downarrow$ value is in line with theory[24] considering the large slanting Zeeman field of $>0.6\ T\,\mu m^{-1}$ of the micromagnet, although shorter than those reported for devices without micromagnets[31]. Regarding the spin as a two-level system weakly coupled to a bath in thermal equilibrium

with $T_\downarrow/T_\uparrow = \exp(-E_Z/kT_B)$, we find the bath temperature $T_B \approx 0.5\ K$ to be significantly higher than the electron temperature $T_e \approx 120\ mK$ measured by Coulomb blockade. This level of heating is reasonable because we observe that the electron temperature increases as the repetition frequency of the pulse for the QND protocol is increased. Heating could be reduced by either reducing the frequency or by increasing the dot-to-gate capacitive coupling so that the pulse amplitude can be decreased. Irrespective of these further precautions, the value of $T_\downarrow$ is almost unaffected by the protocol, evidencing the QND character of our measurement: the evolution of the measured observable is perturbed negligibly by the back action of the measurement or by undesired interactions[2,14].

To summarize, we have implemented QND measurement of a single-electron spin qubit via an ancillary singlet–triplet qubit in an array of GaAs gated quantum dots. The protocol consisting of 60 consecutive cycles (ancilla measurements) realizes a single-spin measurement with fidelity of 89%, and the probability of undesired disturbance in a single cycle is estimated to be less than 0.3%. We expect that the application of this technique to silicon spin qubits will enable qubit readout with high fidelity, well beyond the fault-tolerant threshold, opening a promising route towards quantum error correction.

Online content

Any methods, additional references, Nature Research reporting summaries, source data, statements of data availability and associated accession codes are available at https://doi.org/10.1038/s41565-019-0426-x.
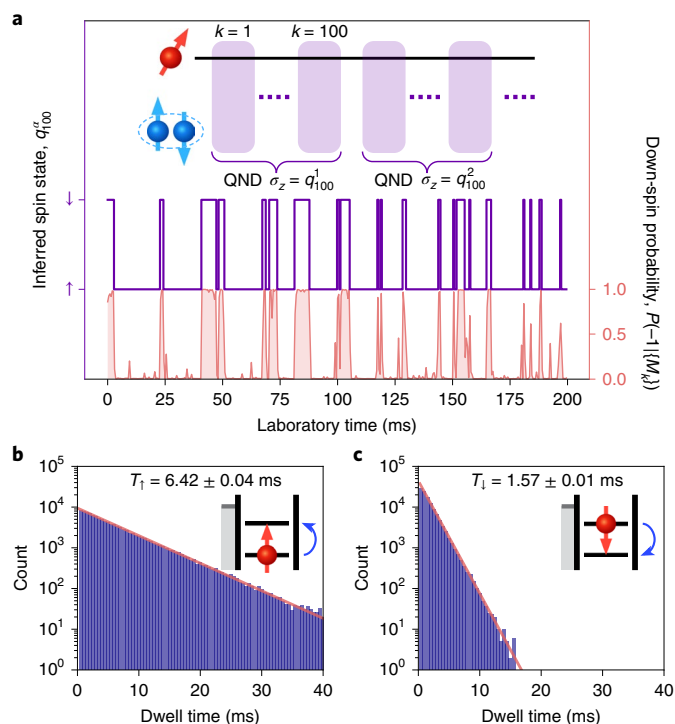
Fig. 4 | Quantum jumps of a single electron spin in a quantum dot.
a, Real-time dynamics of the single spin probed by continuous QND readout. The experiment is performed by skipping the preparation and destructive readout of the single spin in the sequence shown in Fig. 1f and using a QND readout cycle time of 5 μs. The gate conditions are slightly changed from those used in Figs. 2 and 3 so that the single spin is confined more strongly and the ancilla qubit can be initialized faster. The spin-down probability $P(\sigma_z = -1 | \{M_k\})$ is obtained from $n = 100$ readout cycles and plotted in orange. The spin trajectory (purple) is obtained from cumulative estimators q_{100}^α by imposing $P(q_{100}^\alpha | \{M_k\}) > P(-q_{100}^\alpha | \{M_k\}) = 1 - P(q_{100}^\alpha | \{M_k\})$. **b,c**, Histograms of the dwell times in up (**b**) and down (**c**) spin states. Solid lines are fits to the data with exponential decay times $T_{\uparrow,\downarrow}$. Insets, corresponding spin transitions between the Zeeman-split energy levels in a quantum dot.

References

1. Grangier, P., Levenson, J. A. & Poizat, J. P. Quantum non-demolition measurements in optics. *Nature* **396**, 537–542 (1998).
2. Imoto, N., Haus, H. H. A. & Yamamoto, Y. Quantum nondemolition measurement of the photon number via the optical Kerr effect. *Phys. Rev. A* **32**, 2287–2292 (1985).
3. Mehl, S. & DiVincenzo, D. P. Simple operation sequences to couple and interchange quantum information between spin qubits of different kinds. *Phys. Rev. B* **92**, 115448 (2015).
4. Noiri, A. et al. A fast quantum interface between different spin qubit encodings. *Nat. Commun.* **9**, 5066 (2018).
5. Lupascu, A. et al. Quantum non-demolition measurement of a superconducting two-level system. *Nat. Phys.* **3**, 119–123 (2007).
6. Jiang, L. et al. Repetitive readout of a single electronic spin via quantum logic with nuclear spin ancillae. *Science* **326**, 267–272 (2009).
7. Vamivakas, A. et al. Observation of spin-dependent quantum jumps via quantum dot resonance fluorescence. *Nature* **467**, 297–300 (2010).
8. Veldhorst, M. et al. An addressable quantum dot qubit with fault-tolerant control-fidelity. *Nat. Nanotechnol.* **9**, 981–985 (2014).
9. Takeda, K. et al. A fault-tolerant addressable spin qubit in a natural silicon quantum dot. *Sci. Adv.* **2**, e1600694 (2016).
10. Yoneda, J. et al. A quantum-dot spin qubit with coherence limited by charge noise and fidelity higher than 99.9%. *Nat. Nanotechnol.* **13**, 102–106 (2018).
11. Veldhorst, M. et al. A two-qubit logic gate in silicon. *Nature* **526**, 410–414 (2015).
12. Zajac, D. M. et al. Resonantly driven CNOT gate for electron spins. *Science* **359**, 439–442 (2017).
13. Watson, T. F. et al. A programmable two-qubit quantum processor in silicon. *Nature* **555**, 633–637 (2018).
14. Ralph, T. C., Bartlett, S. D., O'Brien, J. L., Pryde, G. J. & Wiseman, H. M. Quantum nondemolition measurements for quantum information. *Phys. Rev. A* **73**, 012113 (2006).
15. Loss, D. & DiVincenzo, D. P. Quantum computation with quantum dots. *Phys. Rev. A* **57**, 120–126 (1998).
16. Elzerman, J. M. et al. Single-shot read-out of an individual electron spin in a quantum dot. *Nature* **430**, 431–435 (2004).
17. Ristè, D., Bultink, C. C., Lehnert, K. W. & Dicarlo, L. Feedback control of a solid-state qubit using high-fidelity projective measurement. *Phys. Rev. Lett.* **109**, 240502 (2012).
18. Neumann, P. et al. Single-shot readout of a single nuclear spin. *Science* **329**, 542–544 (2010).
19. Robledo, L. et al. High-fidelity projective read-out of a solid-state spin quantum register. *Nature* **477**, 574–578 (2011).
20. Pla, J. J. et al. High-fidelity readout and control of a nuclear spin qubit in silicon. *Nature* **496**, 334–338 (2013).
21. Mi, X. et al. A coherent spin–photon interface in silicon. *Nature* **555**, 599–603 (2017).
22. Samkharadze, N. et al. Strong spin–photon coupling in silicon. *Science* **359**, 1123–1127 (2017).
23. Petta, J. R. et al. Coherent manipulation of coupled electron spins in semiconductor quantum dots. *Science* **309**, 2180–2184 (2005).
24. Tokura, Y., van der Wiel, W. G., Obata, T. & Tarucha, S. Coherent single electron spin control in a slanting Zeeman field. *Phys. Rev. Lett.* **96**, 47202 (2006).
25. Yoneda, J. et al. Fast electrical control of single electron spins in quantum dots with vanishing influence from nuclear spins. *Phys. Rev. Lett.* **113**, 267601 (2014).
26. Delbecq, M. R. et al. Quantum dephasing in a gated GaAs triple quantum dot due to non-ergodic noise. *Phys. Rev. Lett.* **116**, 046802 (2016).
27. Gambetta, J., Braff, W., Wallraff, A., Girvin, S. & Schoelkopf, R. Protocols for optimal readout of qubits using a continuous quantum nondemolition measurement. *Phys. Rev. A* **76**, 012325 (2007).
28. Reilly, D. J. et al. Measurement of temporal correlations of the Overhauser field in a double quantum dot. *Phys. Rev. Lett.* **101**, 236803 (2008).
29. Eng, K. et al. Isotopically enhanced triple-quantum-dot qubit. *Sci. Adv.* **1**, e1500214 (2015).
30. Martinis, J. M. Qubit metrology for building a fault-tolerant quantum computer. *npj Quantum Inf.* **1**, 15005 (2015).
31. Amasha, S. et al. Electrical control of spin relaxation in a quantum dot. *Phys. Rev. Lett.* **100**, 046803 (2008).
32. Barthel, C. et al. Fast sensing of double-dot charge arrangement and spin state with a radio-frequency sensor quantum dot. *Phys. Rev. B* **81**, 161308(R) (2010).

Author contributions
T.N., M.R.D. and S.T. conceived and designed the experiments. A.L. and A.D.W. grew the heterostructure. T.N. and A.N. fabricated the device. T.N. and A.N. conducted the experiments with the assistance of K.K. T.N. and A.N. analysed the data and wrote the manuscript with input from J.Y. and P.S. All authors discussed the results and commented on the manuscript. The project was supervised by S.T.

Competing interests

The authors declare no competing interests.

Additional information

Methods

Device design and set-up. The TQD was fabricated on an epitaxially grown GaAs/AlGaAs heterostructure wafer with a two-dimensional electron gas 100 nm below the surface. The Ti/Au gate electrodes deposited on top of the wafer were negatively biased to confine single electrons in each quantum dot and to define the charge-sensing quantum dot. The Co micromagnet was directly placed on the surface and magnetized by the in-plane magnetic field $B_{ext} = 3.155$ T. This was designed to provide a local Zeeman field difference of ~60 mT between the left and centre dots as well as the slanting magnetic field necessary for the selective MM-ESR. At the same time, it provided $\Delta E_Z/(|g|\mu_B) = 40$ mT between the centre and right dots splitting the energy of the $|\uparrow\downarrow\rangle$ and $|\downarrow\uparrow\rangle$ states of the ancilla qubit (g is the electron g-factor and μ_B is the Bohr magneton). The experiment was conducted in a dilution refrigerator with an electron temperature of ~120 mK.

Initialization, manipulation and destructive readout of the single spin are performed within the $(N_L, N_C, N_R) = (1, 0, 2)$ charge configuration, where N_L (N_C, N_R) is the number of electrons in the left (centre, right) quantum dot. The spin is reset to the up-spin ground state by exchanging electrons with the left lead, initialized by the MM-ESR, and read out by the energy-selective tunnelling to the lead. The ancilla qubit is initialized to a doubly-occupied singlet by exchanging electrons with the right lead near the boundary between $(1, 0, 2)$ and $(1, 0, 1)$. The charge configuration is then changed from $(1, 0, 2)$ to $(1, 1, 1)$ by rapid adiabatic passage[33]. Finally, the exchange coupling J to the single-spin qubit is turned on near the $(1, 1, 1)$–$(2, 0, 1)$ charge transition. The ancilla is read out by going back to the $(1, 0, 2)$ region and detecting whether the double occupancy of the right dot is realized or not. If the measured charge state is $(1, 0, 2)$ we assign the ancilla state to be $M = S$, while $M = T$ is found if the system remains in the $(1, 1, 1)$ charge state. See ref. 4 for further details of the device characterization and measurement schemes.

Parameters in $P(M|\sigma_z)$, ϕ^A and ϕ^C. The probability of finding a singlet outcome $M = S$ conditioned on the single spin is ideally given by[4] $P(M = S|\sigma_z) = \langle\sigma S|(Z^S(-\phi^S + \phi^C/2) \otimes Z^A(-\phi^A + \phi^C/2))CZ(-\phi^C)|\sigma S\rangle$, where

$$Z^{\{S,A\}}(\varphi) = \begin{pmatrix} 1 & 0 \\ 0 & \exp(i\varphi) \end{pmatrix}$$

are the phase gates for the single-spin and ancilla qubits, $CZ(\varphi) = |\uparrow\rangle\langle\uparrow| \otimes I + |\downarrow\rangle\langle\downarrow| \otimes Z^C(\varphi)$ is the controlled-Z gate (Z^C acts on the ancilla), and $\phi^S = \frac{E_Z}{\hbar}(\tau' + \tau_R)$ is the precession angle of the single spin independent of the ancilla state (see below for the definitions of τ' and τ_R). Taking into account experimental imperfections, the formula changes into equation (1), where non-ideal ($a < 1/2$) and possibly biased ($b \neq 1/2$) measurement and dephasing ($T_2^* < \infty$) are reflected.

Parameters τ_0 and ϕ_0 in phases ϕ^A and ϕ^C arise in the following way. We write these phases as $\phi^A = \frac{\Delta E_Z}{\hbar}(\tau' + \tau_R) + \phi$ and $\phi^C = \frac{J}{\hbar}(\tau' + \tau_0)$ with $\tau = \tau' + \tau_0$ and $\phi_0 = \Delta E_Z(\tau_R - \tau_0)/\hbar + \phi$. Here, τ' is the controlled time during which the detuning pulse is kept at a constant value inducing a finite exchange coupling J. To avoid state leakage, we turn the exchange coupling J on and off adiabatically, inserting a ramp time $\tau_R/2$ to the beginning and end of detuning pulses. The ramp time $\tau_R = 24$ ns is thus effectively added to τ', contributing to the spin-independent phase ϕ^A. Because J changes nonlinearly during the ramp, the analogous contribution to the spin-dependent phase ϕ^C is written as $J\tau_0/\hbar$ with $\tau_0 \ll \tau_R$. The phase offset ϕ denotes the correction accounting for non-uniform ΔE_Z during the ramp. The values of τ_0, J, ΔE_Z and ϕ are determined from the measured data, as explained in the following.

Among the above parameters, σ_z, ΔE_Z and ϕ vary from record to record due to the projection noise of σ_z and due to random drifts of ΔE_Z and ϕ induced by the magnetic and electric noise. By marginalizing out those (varying) parameters, we first determine the values of the other (constant) parameters using maximum-likelihood estimation. In this way, we find $J = 90.4 \pm 0.3$ MHz, $\tau_0 = 1.54 \pm 0.17$ ns, $a = 0.220 \pm 0.005$ and $b = 0.511 \pm 0.003$. We also find that the value of T_2^* is dependent on the spin state, $T_{2\uparrow}^* = 177 \pm 29$ ns for $\sigma_z = +1$ and $T_{2\downarrow}^* = 212 \pm 57$ ns for $\sigma_z = -1$ (see Supplementary Fig. 2 for the origin of the difference). Once the values of the constant parameters are specified, the drift of ΔE_Z and ϕ is continuously monitored by the Bayesian inference (still marginalizing out σ_z), so that $P(M_k|\sigma_z)$ in equation (1) can be updated after every record. The estimator of σ_z in a record is evaluated using $P(M_k|\sigma_z)$ updated in the preceding record. See ref. 4 for more details of this procedure.

For the data in Fig. 4, where the gate voltage configuration is slightly different, the parameter values are re-estimated to be $J = 84.3 \pm 0.1$ MHz, $\tau_0 = 1.14 \pm 0.06$ ns, $a = 0.220 \pm 0.002$ and $b = 0.501 \pm 0.002$, while $T_{1\uparrow}^*$ and $T_{2\downarrow}^*$ are assumed to be unchanged.

Evolution of the single electron spin. In the sequence shown in Fig. 1f, the single spin is initialized by the microwave burst of duration τ_{mw}. It then freely evolves with t: it precesses coherently around the external magnetic field aligned with the z axis and flips or dephases stochastically due to noise. The probability of the spin to be along z is written as $p_\uparrow(t; \tau_{mw}) = (1 + \langle\sigma_z(t; \tau_{mw})\rangle)/2 = A(t)e^{-(\tau_{mw}/T_2^{Rabi})^2}\cos(2\pi f_{Rabi}\tau_{mw} + \varphi) + B(t)$. It is

insensitive to the precession or dephasing, while spin flips (relaxation or excitation) result in a time dependence of the amplitude $A(t)$ and the offset $B(t)$.

Assuming that the stochastic dynamics can be described as a memoryless process, the spin should follow the rate equation

$$\frac{dp_\uparrow(t)}{dt} = -\frac{1}{T_\uparrow}p_\uparrow(t) + \frac{1}{T_\downarrow}(1 - p_\uparrow(t)) \tag{3}$$

where $T_{\downarrow(\uparrow)}$ is the spin relaxation (excitation) time. Equation (3) leads to $A(t) = A(0)e^{-t/T_1}$ and $B(t) = [B(0) - T_\downarrow/T_\uparrow]e^{-t/T_1} + T_\downarrow/T_\uparrow$ with $T_1^{-1} = T_\uparrow^{-1} + T_\downarrow^{-1}$. Using these formulae, we fit the values of $T_\uparrow$, $T_\downarrow$, $A(0) = 0.298 \pm 0.004$ and $B(0) = 0.616 \pm 0.041$ from the data shown in the inset of Fig. 2c.

Equation (3) also gives $P(\sigma_i|\sigma_{i-1})$, the probability of the spin transition from σ_{i-1} to σ_i between cycles at t_{i-1} and t_i, which is needed in equation (2). Namely, we obtain $P(+1|+1) = e^{-\Delta t/T_\uparrow}$, $P(-1|-1) = e^{-\Delta t/T_\downarrow}$, $P(-1|+1) = 1 - e^{-\Delta t/T_\uparrow}$ and $P(+1|-1) = 1 - e^{-\Delta t/T_\downarrow}$ with $\Delta t = 7$ μs. Note that we define the initial qubit state to be $\sigma_0 = \sigma_1$, that is, $P(\sigma_1|\sigma_0) = \delta_{\sigma_1\sigma_0}$.

Extraction of readout fidelities from joint probabilities. We define the single-readout fidelity as the probability of correctly assigning the estimator to a single spin (fictitiously) initialized to either $\sigma_z(t_k) = +1$ or $\sigma_z(t_k) = -1$ in the kth cycle. The fidelity for the kth QND readout is $f_{\sigma,k}$ and that for the final destructive readout is $f_{q,k}^L$ (Supplementary Fig. 4). Both $f_{\sigma,k}$ and $f_{q,k}^L$ depend on index k, because $f_{\sigma,k}$ is a function of the interaction time τ_k, while $f_{\sigma,k}^L$ is influenced by the spin relaxation taking place during the time interval of $(101 - k) \times 7$ μs before the destructive readout (Fig. 1f). The joint probabilities $P_{m_k \cap m^L}$ of getting an estimator value m_k from the kth QND readout and m^L from the destructive readout are given by

$$P_{+1 \cap +1}(t_k) = f_{\uparrow,k}f_{\uparrow,k}^L p_\uparrow(t_k) + (1 - f_{\downarrow,k})(1 - f_{\downarrow,k}^L)(1 - p_\uparrow(t_k))$$

$$P_{+1 \cap -1}(t_k) = f_{\uparrow,k}(1 - f_{\uparrow,k}^L)p_\uparrow(t_k) + (1 - f_{\downarrow,k})f_{\downarrow,k}^L(1 - p_\uparrow(t_k))$$

$$P_{-1 \cap +1}(t_k) = (1 - f_{\uparrow,k})f_{\uparrow,k}^L p_\uparrow(t_k) + f_{\downarrow,k}(1 - f_{\downarrow,k}^L)(1 - p_\uparrow(t_k))$$

$$P_{-1 \cap -1}(t_k) = (1 - f_{\uparrow,k})(1 - f_{\uparrow,k}^L)p_\uparrow(t_k) + f_{\downarrow,k}f_{\downarrow,k}^L(1 - p_\uparrow(t_k))$$

Note that $P_{m_k \cap m^L} \neq P_{m_k}P_{m^L}$, where P_{m_k} and P_{m^L} are probability distributions of the QND and destructive measurement outcomes, respectively. For each k, we find Rabi oscillations of $P_{m_k \cap m^L}(t_k)$, as shown in Supplementary Fig. 4. The correlation of the two readout schemes is clearly seen as the large oscillation amplitude in the joint probabilities for $m_k = m^L$ while the anticorrelated signals ($m_k \neq m^L$) show only small residual oscillations due to readout errors. By fitting those oscillations, we obtain an overconstrained set of eight equations on $f_{\sigma,k}$, $f_{\sigma,k}^L$, $A(t_k)$ and $B(t_k)$. We derive the most likely values by the least mean squares method for each k, as shown in Fig. 2c.

Theoretical model for readout fidelities. When we perform the kth cycle and find an outcome M_k from the ancilla readout, we assign a correct estimator m_k for $\sigma_z(t_k)$ only if $P(\sigma_z|M_k) - P(-\sigma_z|M_k) > 0$. The success probability $f_{\sigma,k}$ is given by summing $H(P(\sigma_z|M_k) - P(-\sigma_z|M_k))$, with $H(x)$ the Heaviside step function, over all possible ancilla readout outcomes M_k:

$$f_{\sigma,k} = \sum_{M_k} P'(M_k|\sigma_z)H(P(\sigma_z|M_k) - P(-\sigma_z|M_k)) \tag{4}$$

Here, $P'(M_k|\sigma_z)$ describes the probability to realize the outcome M_k at the time of the measurement. It is, in principle, different from $P(M_k|\sigma_z)$ in equation (1), which is the likelihood estimated using the values of ΔE_Z and ϕ obtained from the preceding record. The two probabilities differ due to the drifts of ΔE_Z and ϕ between cycles. We nevertheless approximate $P'(M_k|\sigma_z)$ by $P(M_k|\sigma_z)$. Because these probabilities change with ϕ^A, the values of $f_{\sigma,k}$ vary over time. Averaging over a fluctuating ϕ^A gives $\langle f_{\sigma,k}\rangle$, plotted as solid curves in Fig. 2c.

The fidelity of the cumulative readout using n measurement outcomes is calculated similarly. Equation (4) is generalized to

$$F_{\sigma,n} = \sum_{\{M_k\}} P'(\{M_k\}|\sigma_0)H(P(\sigma_0|\{M_k\}) - P(-\sigma_0|\{M_k\})) \tag{5}$$

Here, $P'(\{M_k\}|\sigma_0)$ is similar to $P(\{M_k\}|\sigma_0)$ in equation (2), but we find noticeable difference between the fidelities in the experiment and simulation when $P'(\{M_k\}|\sigma_0)$ is approximated by $P(\{M_k\}|\sigma_0)$. We therefore additionally take into account the drifts of ΔE_Z and ϕ between different cycles. Rewriting $P(M_k|\sigma_z)$ as $P_{\Delta E_Z,\phi}(M_k|\sigma_z)$ to indicate the dependence explicitly, $P'(\{M_k\}|\sigma_0)$ reads

$$P'(\{M_k\}|\sigma_0) =$$
$$\sum_{\{\sigma_k, \Delta E_{Z,k}, \phi_k\}} \left[\prod_{k=1}^n P_{\Delta E_{Z,k}\phi_k}(M_k|\sigma_k)P(\sigma_k|\sigma_{k-1})P(\Delta E_{Z,k}|\Delta E_{Z,k-1}) \right.$$
$$\left. P(\phi_k|\phi_{k-1}) \right]$$

We model the drifts by the Gaussian random walks as

$$P(\Delta E_{Z,k}|\Delta E_{Z,k-1}) \propto \exp\left[-\frac{(\Delta E_{Z,k}-\Delta E_{Z,k-1})^2}{2h^2\sigma_f^2}\right] \text{ and } P(\phi_k|\phi_{k-1}) \propto \exp\left[-\frac{(\phi_k-\phi_{k-1})^2}{2\sigma_\phi^2}\right]$$ (see

Supplementary Fig. 1 and Supplementary Section 1 for the values of σ_f^2 and σ_ϕ^2). The theoretical values of $F_{\sigma,n}$ plotted in Fig. 3c are calculated by simulating 10,000 numerically generated random sets of outcomes $\{M_k\}$, each corresponding to a set of random trajectories with $\Delta E_{Z,k}$, ϕ_k and σ_k evolving according to $P(\Delta E_{Z,k}|\Delta E_{Z,k-1})$, $P(\phi_k|\phi_{k-1})$ and equation (3), respectively.

Observation of quantum jumps. For the data in Fig. 4, each cumulative estimator q_{100}^α is obtained imposing $P(q_{100}^\alpha|\{M_k\}) > P(-q_{100}^\alpha|\{M_k\})$ for the αth record of $n = 100$ cycles. Bayes' theorem gives $P(\sigma_\alpha|\{M_k\}) = P(\{M_k\}|\sigma_\alpha)P(\sigma_\alpha)/P(\{M_k\})$. Without prior knowledge of σ_α, meaning $P(\sigma_\alpha = +1) = P(\sigma_\alpha = -1) = 1/2$, the readout fidelity expected in our experiment remains at most 0.89, as discussed in the main text. The imperfect fidelity leads to observation of fake quantum jumps as well as $T_\uparrow$ and $T_\downarrow$ values somewhat smaller than those presented in Fig. 4b,c.

To account for these readout errors, we use the prior probability $P(\sigma_\alpha) = P(\sigma_\alpha|\sigma_{\alpha-1})P(\sigma_{\alpha-1})$, where $P(\sigma_\alpha|\sigma_{\alpha-1})$ is the spin flip probability between records and $P(\sigma_{\alpha-1})$ is the probability distribution obtained in the previous record. Here, $P(\sigma_\alpha|\sigma_{\alpha-1})$ is given by $P(+1|+1) = e^{-n\Delta t/T_\uparrow}$, $P(-1|-1) = e^{-n\Delta t/T_\downarrow}$, $P(-1|+1) = 1-e^{-n\Delta t/T_\uparrow}$ and $P(+1|-1) = 1-e^{-n\Delta t/T_\downarrow}$ with $\Delta t = 5\,\mu s$. We initially use the values of $T_\uparrow$ and $T_\downarrow$ extracted as in the above, calculate the estimators and re-extract the values of $T_\uparrow$ and $T_\downarrow$. After repeating this procedure a few times, we find that the values of $T_\uparrow$ and $T_\downarrow$ converge to the result shown in Fig. 4. We tested this procedure in numerical simulations and confirmed that it gives a reliable estimate of $T_\uparrow$ and $T_\downarrow$.

Data availability
The data that support the plots within this paper and other findings of this study are available from the corresponding author upon reasonable request.

References
33. Taylor, J. et al. Relaxation, dephasing and quantum control of electron spins in double quantum dots. *Phys. Rev. B* **76**, 035315 (2007).